J. Non-Newtonian Fluid Mech. 166 (2011) 12–24

Contents lists available at ScienceDirect

Journal of Non-Newtonian Fluid Mechanics

journal homepage: www.elsevier.com/locate/jnnfm

Extrudate swell of linear and branched polyethylenes: ALE simulations and comparison with experiments

Vivek Ganvir[a,b,*], B.P. Gautham[a], Harshawardhan Pol[c], M. Saad Bhamla[d], Lino Sclesi[e], Rochish Thaokar[b], Ashish Lele[c], Malcolm Mackley[e]

[a] Tata Research Development and Design Centre, Pune, India
[b] Department of Chemical Engineering, Indian Institute of Technology Bombay, Mumbai, India
[c] Polymer Science and Engineering Division, National Chemical Laboratory, Pune, India
[d] Department of Chemical Engineering, Indian Institute of Technology Madras, Chennai, India
[e] Department of Chemical Engineering, University of Cambridge, UK

ARTICLE INFO

Article history:
Received 17 May 2010
Received in revised form 1 October 2010
Accepted 5 October 2010

Keywords:
Extrudate swell
ALE-FEM
XPP
PTT
MultiPass Rheometer
Flow birefringence
PSD

ABSTRACT

Extrudate swell is a common phenomenon observed in the polymer extrusion industry. Accurate prediction of the dimensions of an extrudate is important for appropriate design of dies for profile extrusion applications. Prediction of extrudate swell has been challenging due to (i) difficulties associated with accurate representation of the constitutive behavior of polymer melts, and (ii) difficulties associated with the simulation of free surfaces, which requires special techniques in the traditionally used Eulerian framework. In a previous work we had argued that an Arbitrary Lagrangian Eulerian (ALE) based finite element formulation may have advantages in simulating free surface deformations such as in extrudate swell. In the present work we reinforce this argument by comparing our ALE simulations with experimental data on the extrudate swell of commercial grades of linear polyethylene (LLDPE) and branched polyethylene (LDPE). Rheological behavior of the polymers was characterized in shear and uniaxial extensional deformations, and the data was modeled using either the Phan–Thien Tanner (PTT) model or the eXtended Pom–Pom (XPP) model. Additionally, flow birefringence and pressure drop measurements were done using a 10:1 contraction–expansion (CE) slit geometry in a MultiPass Rheometer. Simulated pressure drop and contours of the principal stress difference were compared with experimental data and were found to match well. This provided an independent test for the accuracy of the ALE code and the constitutive equations for simulating a processing-like flow. The polymers were extruded from long ($L/D = 30$) and short ($L/D = 10$) capillaries dies at 190 °C. ALE simulations were performed for the same extrusion conditions and the simulated extrudate swell showed good agreement with the experimental data.

1. Introduction

This paper is concerned with simulations of axisymmetric extrudate swell of polymer melts using an Arbitrary Lagrangian Eulerian (ALE) finite element technique and validating the predictions with experimental data. Predictions of extrudate swell of polymer melts are important for accurate design of dies in profile extrusion applications. Similarly, accurate predictions of extrudate swell can help in optimizing the rheology and hence the molecular structure of polymers so as to suit a given profile extrusion application. In general, the prediction of extrudate swell is a challenging task due to two reasons: (i) there are difficulties associated with incorporating complex constitutive equations in a numerical framework, and (ii) there are difficulties associated with the simulation of free surface, which requires special techniques in the traditionally used Eulerian framework. The degree of extrudate swell depends on the nonlinear viscoelastic properties such as the shear and the extensional viscosities and the first normal stress difference, which are modeled by complex constitutive equations.

Conventionally, the flow properties of polymer melts are characterized by viscometric flows, and the rheological data so obtained is used to fit differential or integral phenomenological constitutive equations [1,2]. These constitutive equations are then used for simulations of complex viscoelastic flow. One of the most widely used constitutive equation for modeling viscoelasticity of polymer melts is the integral K-BKZ equation. Considerable success in modeling viscoelastic flows has been achieved using the Wagner damping function [3] and the Papanastasiou damping function [4] in the K-BKZ integral equation. Another widely used constitutive equation is the differential Phan–Thien Tanner (PTT) equation. With the development of newer constitutive models such as the Pom–Pom model

* Corresponding author at: Tata Research Development and Design Centre, Pune, PEG, 54B, Hadapsar I E, Pune, India. Tel.: +91 20 66086204; fax: +91 20 66086399.
E-mail address: vivek.ganvir@tcs.com (V. Ganvir).

0377-0257/$ – see front matter.
doi:10.1016/j.jnnfm.2010.10.001

[5] or the RoliePoly model [6], which are based on coarse-grained macromolecular architecture and the topological interactions of polymer chains in a mean field sense, researchers have successfully started incorporating them in numerical frameworks to simulate complex polymer flows. This provides an opportunity to relate the performance of processing flows to molecular attributes. Both phenomenological and molecular constitutive equations such as the PTT and XPP have proved to be useful predictive tools for extrudate swell problem [7].

The multi-mode K-BKZ equation was used to predict extrudate swell from long dies for a LDPE melt [8], and enhanced swelling from short dies for the same LDPE [9]. Luo and Tanner [8] introduced the Streamline Finite Element Method (SFEM) which offers a simple algorithm suitable for extrusion operations. SFEM was further modified by Luo and Mitsoulis [10,11]. They introduced particle-tracking on the streamline by using Picard iterative scheme which decouples the computation of the free surface shape from that of the velocity and the stress fields. The authors showed that linear polymer melts, such as LLDPE and HDPE have reduced swelling and vortex behavior compared with a branched LDPE melt. They also showed that the simulated birefringence patterns in flows through short and long dies were in favorable comparison with experiments. Several features of the earlier numerical method of Luo and Mitsoulis [12] were modified by Goublomme et al. [13,14] to simulate flow at high shear rates. Kiriakidis and Mitsoulis [15] studied die swell of HDPE through planar and axisymmetric die using K-BKZ model. Their simulated results showed that for the same shear rate swelling is higher from capillary than slit dies with the same length/diameter ratio. Ahmed et al. [16] simulated the flow of two HDPE melts and one LDPE melt using again a K-BKZ equation. The results of Ahmed et al. [16] highlighted the difficulties in simulating viscoelastic flow and extrudate swell of strongly strain hardening materials, for which the measurement of extensional data and choice of appropriate constitutive equations are necessary. Béraudo et al. [17] addressed this issue by using shear and extensional data to fit a multi-mode Phan–Thien Tanner model for LLDPE and LDPE melts. They used a finite element method based on Newton's iterative scheme and discontinuous approximations of the extra-stress tensor. The free surface was computed by the predictor corrector technique based on streamline method, and only steady state swell simulation was possible. For the LLDPE, their results were in quantitative agreement with available data. However for the LDPE melt, the W-shaped fringes observed right after the downstream channel entrance in flow birefringence experiments were only predicted qualitatively. Also, they did not compare the predicted swell results with experiments.

Bishko et al. [18] performed transient flow simulations of a low-density polyethylene (LDPE) melt through a 4:1 planar contraction with a single-mode Pom–Pom model. Lee et al. [19] used a multi-mode Pom–Pom model to simulate a contraction–expansion flow and showed that the model could discriminate between the flow patterns produced by polymers with various levels of branching. Verbeeten et al. [20] indicated that there are numerical difficulties associated with the mathematical formulation of the Pom–Pom (PP) model which might limit its use in simulating complex flows. They proposed a modified formulation of the Pom–Pom model, referred to as eXtended Pom–Pom (XPP) model. Despite some success, the XPP model has been shown to only partly resolve the original model's shortcomings. Subsequently, Clemeur et al. [21] developed the Double Convected Pom–Pom (DCPP) model with an approach similar to that suggested by Verbeeten et al. [20]. The DCPP model has several advantages; in particular, the prediction of steady extensional viscosity does not show oscillations as observed with the Pom–Pom model when a non-vanishing second normal stress difference (N_2) is incorporated. Clemeur et al. [21] implemented the DCPP model in POLYFLOW^{TM} [22,23] to study complex polymer flow and extrudate swell for branched and linear polymers. Their results on the computed PSD data showed good match with the experimental birefringence data. However, they did not compare calculated swell with the experiments. Recently, Russo and Phillips [24] simulated extrudate swell behavior of branched polymer melts in a planar configuration, using the third order conditionally stable Adams–Bashforth method. The multi-mode eXtended Pom–Pom (XPP) constitutive model was used to describe the rheology of the polymer melts and the simulated results were compared with the experimental data of Meissner [25] on IUPAC-LDPE samples A, B and C and that of Yang et al. [26] on linear low density polyethylene (LLDPE). The predicted swell ratios using the multi-mode XPP model were in good agreement with experiments with the branched IUPAC-LDPE A, B and C samples. However, simulated swell ratios using the XPP model were unable to predict the experimental observed swell for LLPDE [24].

Simulating extrudate swell in a Lagrangian framework is advantageous since the free surface evolves naturally with material flow. However, there are problems associated with mesh distortion, and frequent remeshing is often required. An Arbitrary Lagrangian Eulerian (ALE) formulation can potentially address these problems because of its ability to combine the advantages of both Lagrangian and Eulerian frameworks. We have developed a fractional step ALE based finite element algorithm and have demonstrated its utility for the prediction of the salient corner vortex formed during the flow of polymer solutions in abrupt contractions [27] and the prediction of extrudate swell of polymer melts [28]. In both these works, phenomenological constitutive equations such as the PTT and Oldroyd-B were used in the ALE code. We are interested in incorporating the newer constitutive relations such as those derived from the Pom–Pom model in our ALE code so as to enable the possibility of linking processing behavior of polymer melts with molecular parameters at least at a coarse grained level.

In this work we build on our previous efforts by (a) providing a more rigorous experimental validation of our code, and (b) incorporating the XPP model in our code. We first present experimental data and matching ALE simulations for the flow of a linear polyethylene (LLDPE) melt through (i) a contraction–expansion (CE) slit die, and (ii) out of axisymmetric long and short capillary dies. The simulations were done using the multi-mode Phan–Thien Tanner (PTT) constitutive equation for the LLDPE melt in continuation of our previous work. Next, we simulate the flow of a branched polyethylene melt through the same geometries viz., the CE slit die and the axisymmetric capillary dies, using the ALE code with the multi-mode XPP constitutive model. The XPP model was used for LDPE simulations because it did a far better job of fitting viscometric data in shear and extension compared to the PTT model. Again, the ALE predictions of flow birefringence and extrudate swell are compared with experimental results.

The rest of the paper is organized as follows. In Sections 2 and 3 respectively, the experimental procedure and the numerical method are presented. The equations of the constitutive models are recalled in Section 4. The main results of the paper are presented in several sub-sections in Section 5. These include the estimation of PTT and XPP model parameters, experimental validation of ALE simulations of flow in a contraction–expansion slit die, and comparison of extrudate swell simulation results with experimental data. Section 6 summarizes the salient conclusions of this work.

2. Experimental methods

2.1. Material characterization

Two commercial polyethylenes (PEs), LLDPE (Dowlex 2045G) and LDPE 170A supplied by Dow Chemicals (USA), were used

Table 1
Molecular weights and ^{13}C NMR data for LDPE and LLDPE.

Material	PE type	Mn	Mw	Mz	PDI	Rg	LCB/1000 C-atoms	Characteristic relaxation time at 190 °C (s)
170A	LDPE	30,600	185,900	528,400	6.07	16.40	3	0.333
2045G	LLDPE	46,800	155,200	491,200	3.31	18.46	–	0.01

in this study. Molecular weight distribution (MWD) and average molecular weights were obtained by high temperature gel permeation chromatography (HT-GPC) using PolymerLabs PL-GPC 220 equipped with refractive index, viscometric and light scattering detectors. For HT-GPC experiments, tri-chloro-benzene (TCB) at 135 °C was used as the solvent for dissolving the linear and branched PEs. The HT-GPC results are summarized in Table 1. The LLDPE has a narrower molecular weight distribution than the LDPE. The average degree of long chain branching was determined from ^{13}C NMR spectra using Randall's method [29]. NMR spectra were obtained using a Bruker AV (500 MHz) spectrometer. The PEs were dissolved in ortho-dichlorobenzene containing benzene d_6. CP-MAS and DEPT spectra were obtained at 135 °C. The results are summarized in Table 1. LDPE 170A showed on an average three long chain branches (LCB) per 1000 carbon (C) atoms, while the LLDPE did not show any detectable LCB.

2.2. Rheological characterization

2.2.1. Linear rheology

Storage modulus $G'(\omega)$ and loss modulus $G''(\omega)$ were obtained from small amplitude oscillatory shear experiments, performed using a 25 mm parallel plate geometry on an Anton Paar MCR 301 rheometer. Data was obtained at several temperatures ranging from 150 °C to 240 °C and was shifted to reference temperatures of 150 °C, 170 °C and 190 °C using the time–temperature superposition principle. These reference temperatures were chosen because the uniaxial extensional measurements, the flow birefringence measurements and the extrudate swell measurements were performed at these respective temperatures as explained later. Characteristic relaxation times at 190 °C were obtained from the inverse of the crossover frequency and are shown in Table 1. Creep and recovery experiments were also performed at 150 °C and 190 °C. Steady state compliance and zero shear viscosity (ZSV) were deduced from the creep data. An eight-mode discrete relaxation spectrum was found to be adequate to model the linear and nonlinear viscometric data of the two polymers. As an independent check the ZSV calculated from the relaxation spectrum as $ZSV = \sum \lambda_i G_i$, where λ_i relaxation time and G_i is the relaxation modulus for ith mode, was compared with the ZSV obtained from creep data and was found to be in good agreement. For example ZSV for LDPE-170A at 190 °C, calculated from the spectrum was 42,580 Pa s while the ZSV estimated from creep data was 41,800 Pa s.

2.2.2. Nonlinear rheology

2.2.2.1. Steady shear and step shear. Steady shear and step shear experiments were performed using the Anton Paar MCR 301 rheometer. Steady shear experiments were performed at 190 °C using a cone and plate geometry (25 mm diameter, 2° cone angle) by ramping the shear rate from 0.01 to 10 s^{-1}. The first normal stress difference was also obtained from normal force measurements. Step shear experiments were performed using 25 mm parallel plate geometry at 150 °C for shear rates of 0.01, 0.03, 0.1, 0.3, 1.0 and 3.0 s^{-1}. For higher shear rates (>3 s^{-1}), the transient viscosity data was not reliable since the specimen was forced out from the gap between the parallel plates.

2.2.2.2. Uniaxial extensional rheology. The transient uniaxial extensional rheology measurements were carried using an ARES rheometer equipped with the Sentmanat Extensional Rheology (SER) fixture. In the SER fixture 6.5 mm wide × about 300 μm thick rectangular polymeric film specimens were fixed with clamps on two counter-rotating cylindrical drums, which are used to wind up the sample. While one cylinder (master drum) is driven by the ARES motor, the other (slave drum) rotates in the opposite direction and is directly coupled with the torque transducer of the ARES to measure the torque, T, on the sample. The force, F, on the sample was calculated from the measured torque by dividing it by the cylinder radius, R. For a constant drive shaft rotation rate, Ω, the Hencky strain rate, $\dot{\varepsilon}_h$, applied to the sample specimen can be expressed as: $\dot{\varepsilon}_h = 2\Omega R/L_0$, where R is the radius of the equal dimension windup cylinders, and L_0 is the fixed, unsupported length of the specimen sample being stretched, which is equal to the centerline distance between the master and slave cylinder drums.

During the experiment, the reactive force on the transducer was measured as a function of time or deformation. The transient uniaxial elongational viscosity, η_E^+, was calculated from the measured force and the applied Hencky strain rate. For the present case, SER measurements were performed at Hencky strain rates of 0.1, 0.3, 1.0, 3.0, and 10.0 s^{-1} and at a temperature of 150 °C. Corrections were made for force base line drift and start time error. The nominal strain rate was assumed to be equal to the actual strain rate. A few experiments were video recorded and the true strain measured from the images was found to be in close agreement with the nominal strain.

2.3. Flow birefringence experiments using MultiPass Rheometer (MPR)

Experimental flow birefringence data was obtained using a Cambridge MultiPass Rheometer [30], with an optical configuration that has been previously described by Collis et al. [31]. The MPR is a dual-piston capillary-type rheometer designed for small quantities of material. In the MPR experiment the material can be repeatedly passed through the midsection, from one reservoir to the other and back again at different flow rates. Pressure drop across the midsection is measured in each pass using two transducers that are flush mounted at either ends of the slit. The geometry of the mid section used in this work was a 10:1 contraction–expansion (CE) slit geometry with rounded corners and short slit length (Fig. 2). The flow consists of regions of high shear near the slit walls, a predominantly extensional component in the entrance region of the slit and a decelerating region at the end of the slit. The flow resembles the more complex industrial processing situations, however the planar geometry enables flow birefringence studies for which a monochromatic circularly polarised light of 514 nm wavelength was passed along the vorticity direction through the midsection and an orthogonal analyser before being captured using a digital video camera. Experiments were performed for both polyethylene samples at 170 °C. The path length for the light in the midsection was equal to the depth of the geometry, viz. 10 mm, which gave a 10:1 width:depth ratio for the slit and a 1:1 width:depth ratio upstream and downstream of the slit. Thus the flow is quasi-2D in the slit and 3D upstream and downstream of the slit.

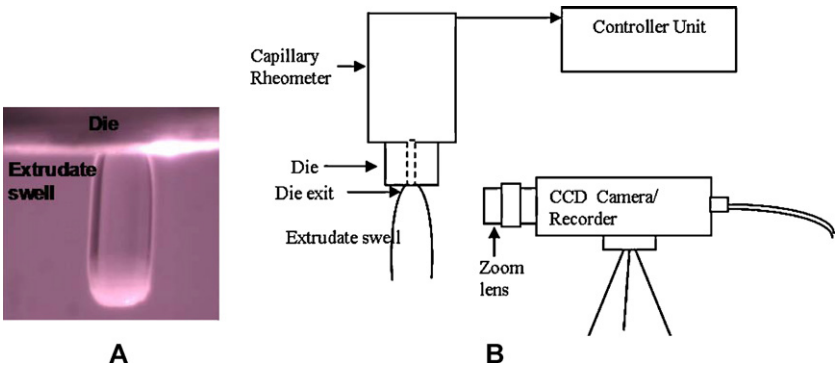

Fig. 1. (A) Captured image of extrudate profile and (B) schematic of experimental setup for extrudate swell.

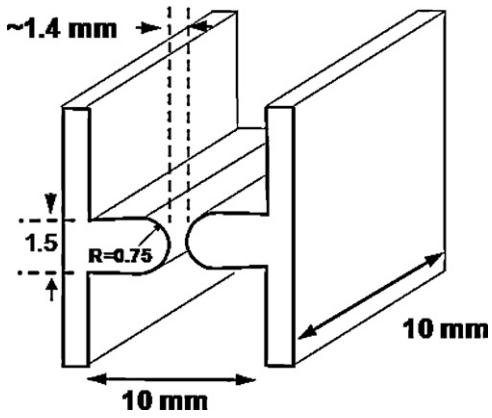

Fig. 2. Schematic of a 10:1 CE slit die with rounded corners and short slit.

2.4. Extrudate swell

Extrusion experiments for LDPE-170A and LLDPE-2045G melt were performed using a CEAST Capillary Rheometer (Model 2100) fitted with axisymmetric capillary dies (Fig. 1(A)). The rheometer was run with an in-house developed LabView based data acquisition and control system. The polymers were extruded through the capillary dies at 190 °C and at various piston speeds (u) that ranged between 0.004 and 0.08 mm/s, which corresponded to apparent wall shear rates in the range 1.6–32 s^{-1} as given by $\dot{\gamma}_a = 4R_b^3 u/R^3$, where R_b and R are respectively the radii of the barrel and the die. Two axisymmetric dies of diameter (D) 2 mm and die lengths (L) 20 mm and 60 mm were used in the experimental study. The geometric characteristics of the two dies are given in Table 2. The axisymmetric dies have a contraction ratio of 10:1. Beyond an apparent wall shear rate of ~40 s^{-1}, flow instabilities like shark skin for LLDPE and melt facture for LDPE were noticed, and experiments were not performed above these shear rates.

The images of the polymer melt extrudate coming out of the capillary dies were captured by a commercial CCD camera (Lumenera Corp., Canada) and a DVD recorder (Onida Ltd., India). The CCD camera fitted with a macrozoom lens was focused on the region near the die exit in order to obtain a 2D image of the extrudate profile of the polymer melt. An example image of the extrudate profile is shown in Fig. 1(B). Extrudate swell profiles were obtained from the images using the image processing software ImageJ (USA). The conventional definition of extrudate swell ratio namely, the ratio of the extrudate diameter and die diameter was used for quantification. In a different set of experiments, the extruded strands were quenched by collecting them in water at ambient temperature. The solidified extrudate strands were then cut and utilized for equilibrium swell measurements. Equilibrium swell was measured by immersing the cut extrudate strands in a hot silicone oil bath at 160 °C for 5 min and then quickly recording the dimensions of the swollen molten strands before they re-solidified.

3. Numerical modeling

Numerical simulations of 2D isothermal flow were carried out using a fractional step ALE based finite element technique. The geometry and the boundary conditions for simulations are shown in Figs. 3(A) and 4(A) respectively for the axisymmetric die and the CE slit die. The ALE technique was discussed in Ganvir et al. [27] and details of simulations of extrudate swell using the ALE algorithm were described in our previous work [28]. A brief description is provided below for the sake of completeness.

The simulation domain comprised the die geometry, which is a spatially fixed window, and the free surface flow after the die exit (Fig. 3A), where the mesh is allowed to move. No slip boundary conditions are applied on the die wall and fully developed flow boundary condition is assumed at the inlet of the die. For free surface analysis, we assume at the beginning of the simulation the existence of an extrudate of the same radius as the die exit and of finite length. A zero force boundary condition is considered on the free surface. In the first step of the ALE simulation the flow is analyzed in the Lagrangian mode i.e., the mesh is moved with the material. In the second step the mesh is moved arbitrarily as required by the flow domain. Inside the fixed window (die) we impose zero velocity for mesh motion at all nodes. This implies that the mesh is moved back to its original position at every time step. The nodes in the extrudate zone are allowed to move with the material motion ($\boldsymbol{v}$) in the Y direction. The mesh velocity ($\boldsymbol{v}_\mathbf{m}$) of a node is computed from the relative motion between its present location and its earlier position at every time step. The convective velocity $\boldsymbol{c}$ is given by $\boldsymbol{v} - \boldsymbol{v}_\mathbf{m}$. In this way the free surface is evolved with material flow and mesh distortion related problems were effectively tackled.

Table 2
Geometric characteristics of the long and short capillary dies.

Geometry	Die	Die length (L) (mm)	Diameter (D) (mm)	L/D	Contraction ratio
Axisymmetric	Short	20	2	10	10:1
Axisymmetric	Long	60	2	30	10:1

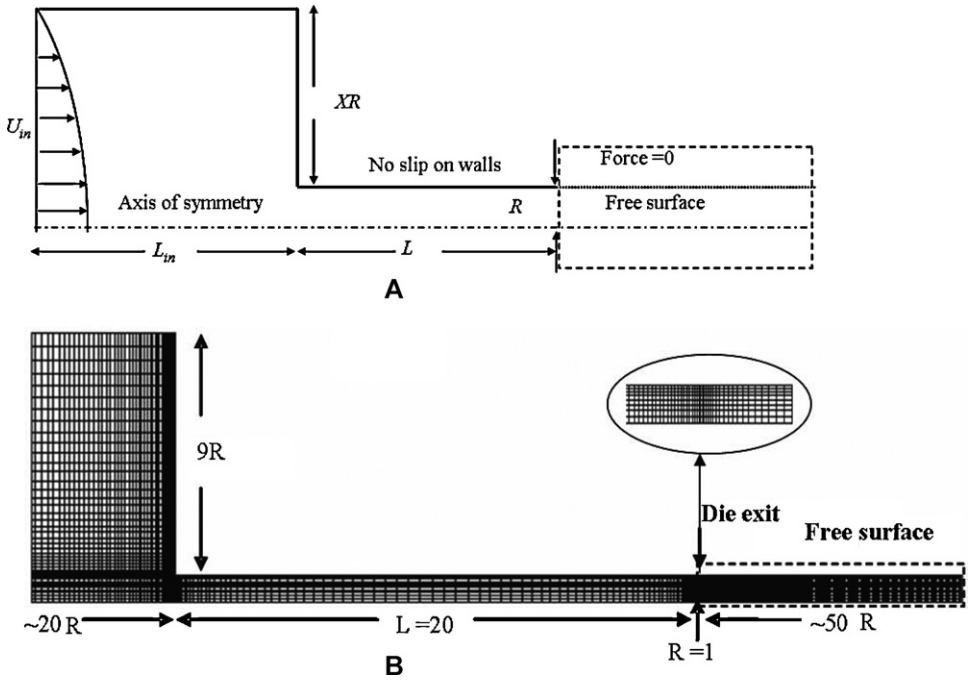

Fig. 3. (A) Die geometry, 10:1 axisymmetric contraction with 1 mm radius and (B) typical mesh with quadratic elements representing the short die used for simulation.

Simulations were performed at the same apparent wall shear rates as those used in experiments, and are defined for the planar slit and the axisymmetric capillary geometries in the standard way namely, $\dot{\gamma}_{w,app} = 6\pi R_b^2 U_{in}/W(2h)^2$ and $\dot{\gamma}_{w,app} = 4\pi R_b^2 U_{in}/R^3$, respectively. Here $2h$ is the slit gap, W is width of the slit, U_{in} is the average velocity in the barrels of the capillary and MPR rheometers, R_b is the radius of the barrels and R is the radius of the capillary die.

The flow domains were divided into quadratic elements, with quadratic velocity and linear pressure interpolation functions. The meshes created for extrudate swell studies and stress birefringence studies are shown in Figs. 3(B) and 4(B), respectively. The pressure nodes were discontinuous and located at four Gauss points. Computation of flow was done using standard velocity–pressure mixed formulations for incompressible fluid. The material constitutive equation was solved iteratively by Picard iteration using a

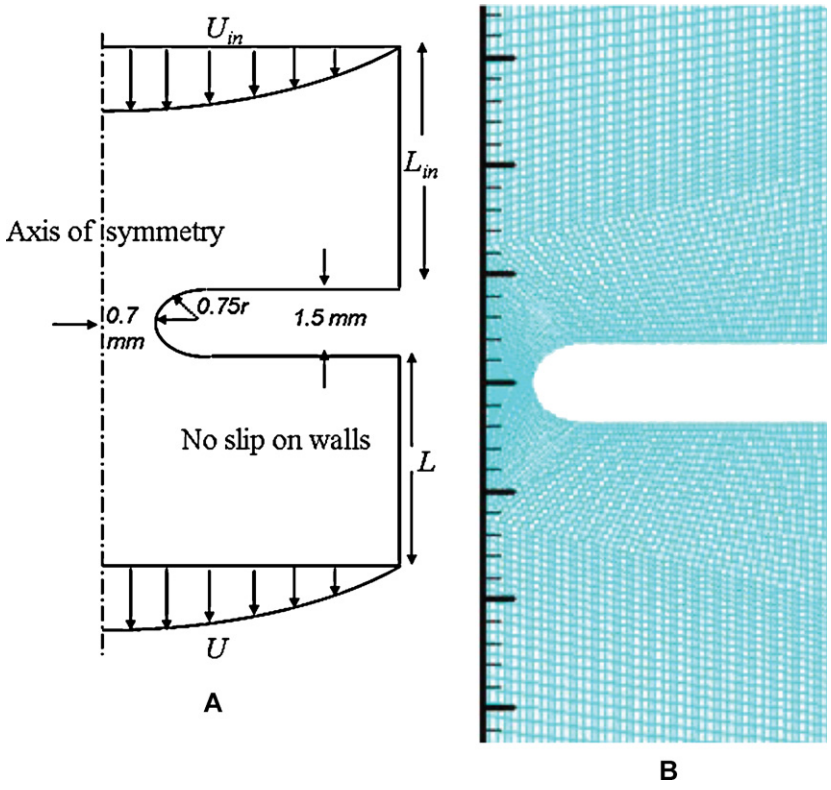

Fig. 4. (A) CE die geometry with boundary conditions and (B) typical mesh with quadratic elements representing the CE die used for simulation.

velocity (v) convergence criterion as given by

$$v_{\text{norm}} = \sqrt{\frac{(v_{i+1}^n - v_i^n)^2}{(v_{i+1}^n)^2}} < 10^{-7} \quad (1)$$

where, the subscript i and the superscript n refer to the iteration and step number, respectively.

Stresses were computed on the Gauss points and the treatment of convection was done by the Godunov update scheme. The time steps used were of the order of 10^{-3} to 10^{-4} s and flow was simulated until it reached steady state.

Following our previous work [28], the convergence of the numerical scheme was tested for the LLDPE polymer using the PTT model by using three different levels of mesh refinement. The smallest elements in the three meshes M1, M2 and M3 were of size 0.04, 0.02 and 0.012 mm. In particular the mesh was refined at the reentry corner of the die and at the die exit because of the existence of stress singularities at these locations (Fig. 3(B)). The stresses were found to be higher at the die exit than at the reentry and hence the mesh was made even finer at the die exit. The value of extrudate swell ratio at steady state for various shear rates was compared to check for convergence. It was found that the swell ratio changed by less than 0.7% when using M3 compared to M2 for two different shear rates, 3.3 s^{-1} and 33 s^{-1}. Consequently in this work we have used a midsize mesh comprising 20,207 nodes and 4794 elements which is finer than the converged mesh (M2) used in our previous work [28].

For this mesh a typical simulation took approximately 100 h to run on a 2 GB Ram, 2.8 GHz Pentium Dual Core processor. The absence of sharp corners in case of the contraction–expansion slit geometry (Fig. 4(A)) avoided difficulties related to stress concentrations in simulations. A mesh (Fig. 4(B)) comprising 1520 elements and 6317 nodes was found to give converged results. A typical simulation took approximately 1 h to run on a 2 GB RAM, 2.8 GHz Pentium Dual Core processor.

4. Governing and constitutive equations

The equations governing the laminar flow of an incompressible viscoelastic fluid are

$$\nabla \cdot \boldsymbol{v} = 0 \quad (2)$$

$$-\nabla p + \nabla \cdot \boldsymbol{\sigma} = 0 \quad (3)$$

where $\boldsymbol{v}$ is the velocity, p is the pressure and $\boldsymbol{\sigma}$ is stress tensor. For a viscoelastic fluid the stress tensor is expressed as a sum of Newtonian and viscoelastic components:

$$\boldsymbol{\sigma} = \boldsymbol{\tau}_s + \boldsymbol{\tau}_v \quad (4)$$

here $\boldsymbol{\tau}_v$ is the extra stress tensor due to viscoelasticity and $\boldsymbol{\tau}_s$ is the stress component of a Newtonian fluid given by

$$\boldsymbol{\tau}_s = \eta_s \boldsymbol{D}; \quad \boldsymbol{D} = (\nabla \boldsymbol{v} + \nabla \boldsymbol{v}^T) \quad (5)$$

The extra stress tensor due to viscoelasticity is then given by

$$\boldsymbol{\tau}_v = \sum \boldsymbol{\tau}_{vi} \quad (6)$$

where, the stress contribution of the ith mode is given by an appropriate constitutive equation. Two differential constitutive equations, the PTT equation for the linear polymer (LLDPE) and the XPP constitutive equation for the branched polymer (LDPE), were used and these are recalled below.

4.1. Phan–Thien Tanner (PTT) constitutive equation

$$\lambda_i \overset{\nabla}{\boldsymbol{\tau}}_{vi} + \exp\left(\frac{\lambda_i \varepsilon}{\eta_{vi}} Tr[\boldsymbol{\tau}_{vi}]\right) \boldsymbol{\tau}_{vi} + \xi(\mathbf{D} \cdot \boldsymbol{\tau}_{vi} + \boldsymbol{\tau}_{vi} \cdot \mathbf{D}) = \eta_{vi} \mathbf{D} \quad (7)$$

here ε and ξ are model parameters. $Tr[\boldsymbol{\tau}_{vi}]$ is the trace of the viscoelastic tensor $\boldsymbol{\tau}_v$, and λ_i and η_{vi} are respectively the relaxation time and viscosity of the ith mode. In Eq. (7) the upper convected derivative $\overset{\nabla}{\boldsymbol{\tau}}_{vi}$ is given by

$$\overset{\nabla}{\boldsymbol{\tau}}_{vi} = \frac{D\boldsymbol{\tau}_{vi}}{Dt} - \boldsymbol{\tau}_{vi} \cdot \nabla \boldsymbol{v} - \nabla \boldsymbol{v}^T \cdot \boldsymbol{\tau}_{vi} \quad (8)$$

4.2. Single equation eXtended Pom–Pom (XPP) model

Following Verbeteen et al. [20] the multi-mode XPP model is expressed in a single equation as follows:

Expression for the stress:

$$\overset{\nabla}{\boldsymbol{\tau}}_{vi} + \lambda_i (\boldsymbol{\tau}_{vi})^{-1} \cdot \boldsymbol{\tau}_{vi} = 2\boldsymbol{G}_{0i}\mathbf{D} \quad (9)$$

Evolution of orientation:

$$\lambda_i (\boldsymbol{\tau}_{vi})^{-1} = \frac{1}{\lambda_{0bi}} \left(\frac{\alpha_i}{G_{0i}} \boldsymbol{\tau}_{vi} + f(\boldsymbol{\tau}_{vi})^{-1} I + G_{0i}(f(\boldsymbol{\tau}_{vi})^{-1} - 1)\boldsymbol{\tau}_{vi}^{-1} \right) \quad (10)$$

Evolution of backbone stretch:

$$\frac{1}{\lambda_{0bi}} f(\boldsymbol{\tau}_{vi})^{-1} = \frac{2}{\lambda_{si}} \left(1 - \frac{1}{\Lambda_i}\right) - \frac{1}{\lambda_{0bi} \Lambda_i^2} \left(1 - \frac{\alpha_i I_{\tau_v \cdot \tau_v}}{3G_{0i}^2}\right) \quad (11)$$

strictly for $\lambda < q$

Timescales:

$$\Lambda_i = \sqrt{1 + \frac{I_{\tau_v}}{3G_0}} \quad (12)$$

$$\lambda_{si} = \lambda_{0si} e^{-\nu_i(\Lambda_i - 1)}, \quad \nu_i = \frac{2}{q_i} \quad (13)$$

In the above equations G_{oi} is the relaxation modulus, λ_{0bi} is the relaxation time of the backbone and λ_{si} is the relaxation time of q_i arms for the ith mode, I_τ is the first invariant (i.e., the trace) of $\boldsymbol{\tau}$, $I_{\tau.\tau}$ is the second invariant (i.e., the trace) of $\boldsymbol{\tau} \cdot \boldsymbol{\tau}$ and α is a scalar parameter. Substitution of Eqs. (13), (12), (11) and (10) in Eq. (9) gives the single equation form which is similar to the multi-mode PTT constitutive equation:

$$\overset{\nabla}{\boldsymbol{\tau}}_{vi} + f(\boldsymbol{\tau}_{vi}, \Lambda_i, q_i).\boldsymbol{\tau}_{vi} = 2G_0\mathbf{D} \quad (14)$$

5. Results and discussion

5.1. Rheological characterization

The relaxation spectra of the two PEs (2045G and 107A) were determined from the time–temperature superposed mastercurves of the storage and loss moduli, $G'(\omega)$ and $G''(\omega)$, using standard linear regression techniques inbuilt in the rheometer software. The discrete eight-mode relaxation spectra were obtained at 150 °C, 170 °C and 190 °C and are given in Tables 3 and 4 respectively for LLDPE and LDPE. A comparison of the relaxation spectra of these two polymer melts at the same temperature showed that the LDPE had broader distribution compared to LLDPE. This is inline with the findings of the HTGPC and ^{13}C NMR techniques; the broader molecular weight distribution and the presence of long chain branching in LDPE causes longer relaxation times.

5.1.1. PTT parameter estimation

The multi-mode PTT model [Eq. (6)] was used to represent the rheology of the linear polymer melt (LLDPE, Dowlex-2045G). The nonlinear parameters ε and ξ of the PTT model were obtained by fitting the constitutive equation simultaneously to the steady shear stress and first normal stress difference data as well as to the transient uniaxial elongation and shear start-up data [16]. The PTT

Table 3
Relaxation spectrum at 150 °C, 168 °C and 190 °C for 2045G LLDPE melt with PTT parameters.

No. of modes (i)	Relaxation spectrum						PTT parameters	
	150 °C		168 °C		190 °C			
	G_i (Pa)	λ_i (s)	G_i (Pa)	λ_i (s)	G_i (Pa)	λ_i (s)	ε	ξ
1	292983.59	0.01	287572.78	0.007	287572.78	0.0048	0.35	0.0
2	66624.44	0.043	70976.63	0.0293	70976.63	0.02	0.35	0.0
3	30450.87	0.183	31897.86	0.124	31897.86	0.0838	0.35	0.0
4	6581.87	0.785	7093.41	0.518	7093.41	0.352	0.35	0.0
5	1200.18	3.362	1347.73	2.175	1347.73	1.474	0.35	0.0
6	167.03	14.397	188.77	9.123	188.77	6.184	0.35	0.0
7	18.69	61.65	23.93	38.27	23.93	25.94	0.35	0.0
8	1.63	263.99	1.91	160.52	1.91	108.81	0.35	0.0

Table 4
Relaxation spectrum at 150 °C, 170 °C and 190 °C for LDPE 170A melt with XPP parameters.

No. of modes (i)	Maxwell parameters						XPP parameters		
	150 °C		170 °C		190 °C				
	G_i (Pa)	λ_{bi} (s)	G_i (Pa)	λ_{bi} (s)	G_i (Pa)	λ_{bi} (s)	$\Gamma_i = \lambda_b / \lambda_{si}$	α_i	q_i
1	93906.53	0.01	94089.33	0.004	94089.33	0.0023	6	04	1
2	31338.38	0.045	31707.59	0.020	31707.59	0.011	5	0.4	1
3	23002.11	0.20	23370.10	0.090	23370.1	0.048	5	0.2	2
4	11435.39	0.91	11565.62	0.408	11565.62	0.217	4	0.2	2
5	5505.88	4.11	5565.85	1.85	5565.85	0.984	3.5	0.117	3
6	1845.06	12.53	2065.41	8.39	2065.40	4.463	3	0.133	4
7	527.83	61.44	536.97	38.07	536.96	20.243	2.5	0.08	5
8	129.04	305.79	160.43	172.67	160.43	91.819	2	0.067	6

model being non-separable, it is not straightforward to arrive at an optimal set of parameters that fit both the steady shear and the transient rheological data. Hence we adopted a two step procedure to obtain the model parameters. In the first step, an optimal parameter fit was obtained by minimizing the deviation from the steady shear experiments with the objective function defined as:

$$q_s = \sum_j \left[\left(\frac{N_{1,j} - N_{1,j}^{\exp}}{N_{1,j}^{\exp}} \right)^2 + \left(\frac{\eta_j - \eta_j^{\exp}}{\eta_j^{\exp}} \right)^2 \right] \quad (15)$$

where, $N_{1,j}^{\exp}$ and $\eta_j^{\exp}$ are experimental values of the first normal stress difference and shear viscosity, respectively.

The above objective function gives several minima. Careful selection of the choice of PTT parameters was therefore guided by earlier studies. Following Macosko [32] $\xi = 0$ was chosen for the LLDPE melt. Consequently, values of ε in the range 0.32–0.38 showed good fit to the steady shear experimental data (Fig. 5 (A)). In the second step the choice of parameter values was fine-tuned by fitting the model to step shear and uniaxial elongational data. The norm of residuals was calculated as $\|p\| = \sqrt{(1/N)\sum_i ([\log(\eta^+_{\exp,i})]^2 - [\log(\eta^+_{\mathrm{fit},i})]^2)/[\log(\eta^+_{\exp,i})]^2}$ for various values of ε and was found to be minimum for $\varepsilon = 0.35$. The fits to the steady shear, step shear and the uniaxial elongational viscosity data are shown in Fig. 5(B). The linear polymer did not display strain hardening and the steady extensional viscosity approached a value three times the steady shear viscosity. The PTT parameters obtained are tabulated in Table 3. Similar, results of PTT fits of steady shear data and first normal stress difference and the step shear and uniaxial extension viscosity was obtained for LDPE-170A are shown in Fig. 6(A) and (B), respectively. The PTT model parameters obtained for LDPE-170A are $\xi = 0.18$ and $\varepsilon = 0.065$. The PTT model provided good fit uniaxial extensional data while it shows oscillations for step shear fit for the branched LDPE-170A melt. Due to oscillations and damping of the PTT model to fit LDPE rheological data, it was decided to employ XPP model for LDPE-170A.

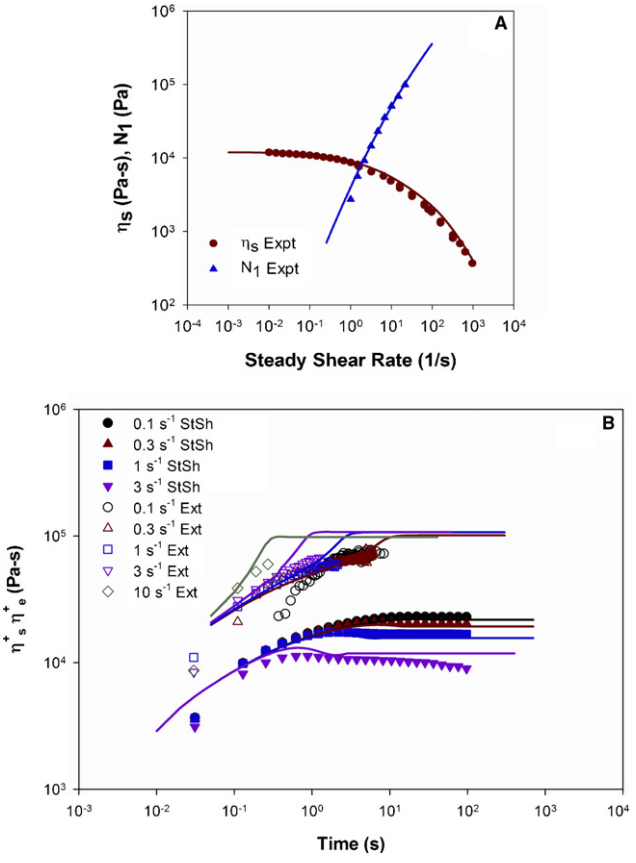

Fig. 5. (A) Steady shear (η_s) and first normal stress difference (N_1) at 190 °C for 2045G LLDPE melt fitted with PTT model and (B) transient uniaxial extensional viscosity (η_e^+) and step shear viscosity (η_s^+) at 150 °C (closed symbols – step-shear data and open symbols – uniax. extensional data); in both figures, lines are PTT fit to data.

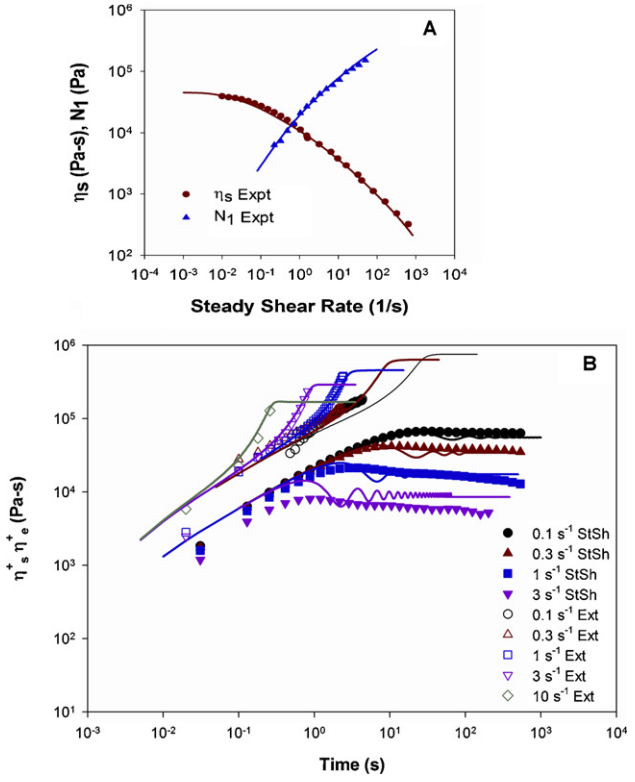

Fig. 6. (A) Steady shear (η_s) and first normal stress difference (N_1) at 190 °C for 170A LDPE melt fitted with PTT model and (B) transient uniaxial extensional viscosity (η_e^+) and step shear viscosity (η_s^+) at 150 °C (closed symbols – step-shear data and open symbols – uniax. extensional data); in both figures, lines are PTT fit to data.

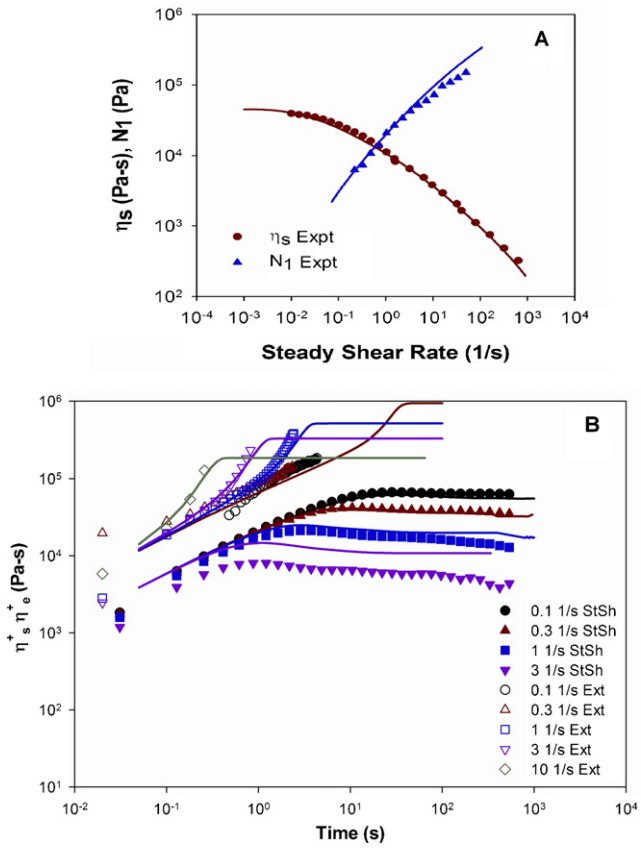

Fig. 7. (A) Steady shear (η_s) and first normal stress difference (N_1) at 190 °C for LDPE 170A melt and (B) transient uniaxial extensional viscosity (η_e^+) and step shear viscosity (η_s^+) at 150 °C (closed symbols – step-shear data and open symbols – uniax. extensional data); in both figures, lines are XPP fit to data.

5.1.2. XPP parameter estimation

The parameters of the XPP model [Eq. (14)] namely, the number of branches (q) and the ratio of backbone relaxation time to branch relaxation time, $\Gamma = \lambda_{0b}/\lambda_{0s}$, represent the structure and hierarchical dynamics of the polymer chains comprising the melt. The nonlinear parameters q_i and $\Gamma_i = \lambda_{b,i}/\lambda_{s,i}$ for all i modes were obtained by fitting the model to the transient uniaxial elongational and the shear start-up data using the guidelines provided by Verbeeten et al. [20]. Following this paper the anisotropy parameter α_i in the XPP model was chosen as $0.4/q_i$. Similarly, a maximum of 6 arms was selected for the longest mode i.e., the 8th mode, the number of arms was decreased with decreasing relaxation time. All the estimated parameters are summarized in Table 4. Fig. 7 shows model fits to experimental rheological data in uniaxial extensional data and step shear data at 150 °C. The parameters were also checked by comparing the model predictions for the steady shear viscosity and the first normal stress difference with experimental data at 190 °C (Fig. 7(B)). In all cases the goodness of fit was decided qualitatively, i.e., visually. The fitting of extensional viscosity data was found to be most sensitive to the number of branches, q, while and the fitting of the step shear data was most sensitive to the ratio of backbone relaxation time to branch relaxation time, $\Gamma = \lambda_{0b}/\lambda_{0s}$.

5.2. Comparison for flow through a 10:1 CE slit

We now compare the predictions of ALE simulations for 2D isothermal flow through a contraction–expansion slit die with experimental data. In particular, the predicted average pressure drop across the die is compared with the measured pressure difference at various flow rates. Additionally, the contours of principal stress difference predicted from simulations are converted to birefringence contours which are compared with the measured birefringence patterns at different flow rates. Here we assume the validity of the stress–optical law given by

$$\Delta n = C\left|\mathrm{PSD}\right| \tag{16}$$

Eq. (16) relates the refractive index Δn to the principal stress difference, i.e., the difference in the eigen values of the stress tensor, by the constant of proportionality C, the stress–optical coefficient, which depends on the chemical structure of the polymer. The value of stress–optical coefficient is taken as 1.47×10^{-9} (Pa^{-1}) for polyethylene [33]. For two-dimensional flows, the stress optical rule can be simplified to give the isochromatic fringe stress (PSD) as

$$\left|\mathrm{PSD}\right| = \sqrt{4\tau_{xy} - (\tau_{xx} + \tau_{yy})^2} = \frac{k\lambda}{dC} \tag{17}$$

here λ is the wave length of the light used in the measurements, d is the path length of light in the birefringent medium (taken equal to the depth of the flow cell), and k the fringe order of the observed dark fringe bands at which extinction of light occurs. Eq. (17) was used to convert the contours of simulated PSD into contours of fringes orders, which were then compared with experimentally observed fringe patterns.

These comparisons provide an independent validation of the predictions of the simulation technique coupled with a constitutive equation. Fig. 8 shows experimental birefringence patterns and those calculated from the simulated principal stress difference contours for the LLDPE melt using the ALE code and the PTT constitutive equation. The shapes of the predicted and observed fringe patterns are in reasonable qualitative agreement. In all the

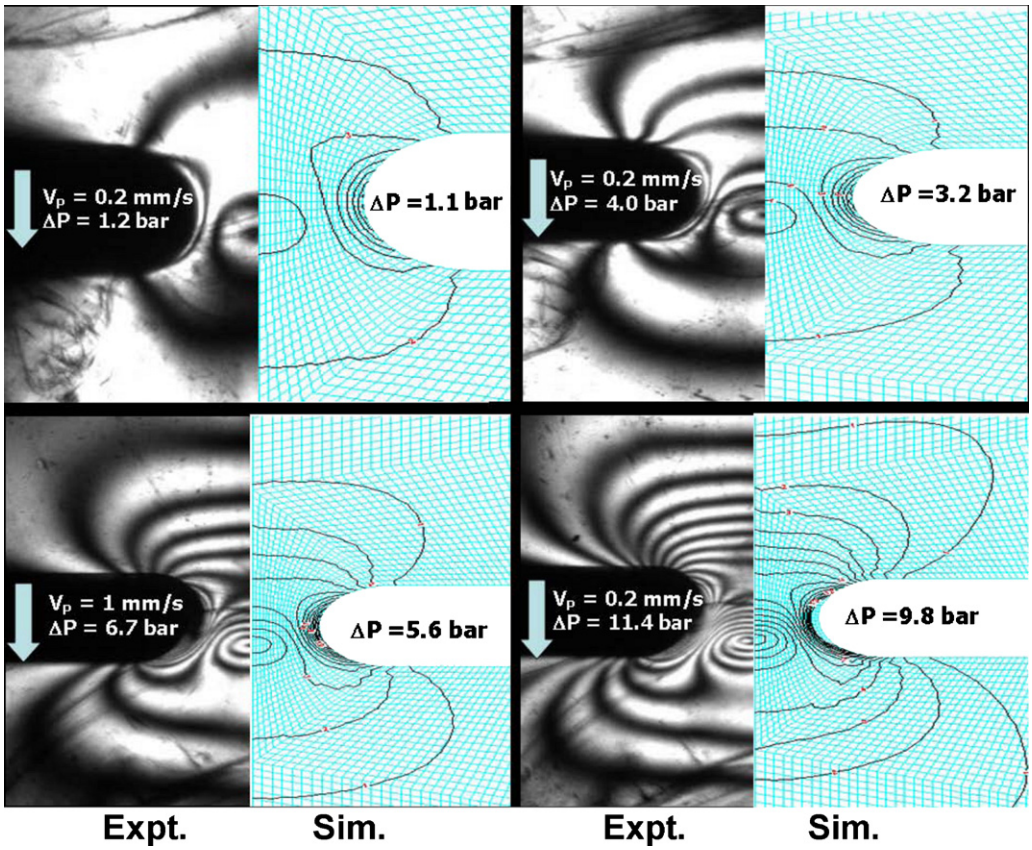

Fig. 8. Comparison of experimental birefringence with principal stress difference contour prediction made by ALE simulations using the PTT model for LLDPE 2045G at 168 °C.

cases the simulated PSD contours showed better agreement with fringes inside the slit compared to those in the main channel. We note that while the simulations are for a two dimensional flow, the experiments are in reality only quasi-two dimensional with the ratio of depth to width of the narrowest part of the slit geometry being 10:1. Thus the poor matching of fringes away from the slit is to a large extent the consequence of the failure of 2D flow assumption in the simulations. The predicted pressure drop is in reasonable agreement with measured values at low flow rates, but at higher flow rates the numerical solution under predicted the measured pressure drop values. The measured and predicted pressure drops are also reported in Fig. 8.

Experimental and simulated birefringence patterns for the LDPE melt are shown in Fig. 9. The predicted patterns are obtained using the XPP constitutive equation in the ALE simulations. The predicted fringe patterns show reasonable match with observed fringes across all flow rates. For a given flow rate the branched LDPE showed more fringes compared to the linear LLDPE. Also, the fringe pattern was very different for the two polymers for any given flow rate. The simulations were largely successful in capturing these features qualitatively. The predicted pressure drops are also in good agreement with the measured values across slit die, and are reported in Fig. 9.

5.3. Extrudate swell simulations and comparison with experiments

Encouraged by the results presented in the previous section we now use the ALE code [28] to simulate extrudate swell, which for an axisymmetric extrudate is defined as [34]

$$\text{Extrudate swell ratio} = \frac{\text{diameter of extrudate}\,(d)}{\text{diameter of die}\,(D)} \tag{18}$$

The temporal evolution of the free surface was simulated till steady state was reached as indicated by no further change of extrudate swell with time. Simulated extrudate swells for LDPE and LLDPE were compared with experimental data at 190 °C.

5.3.1. Linear LLDPE-2045G

5.3.1.1. Extrudate swell predictions for a long capillary die. We first report ALE simulations of extrusion through a long capillary die having length to diameter ratio, $L/D = 30$, and compare the extrudate swell predictions with experimental measurements. As noted earlier, simulations for LLDPE were done using the PTT constitutive model whose parameters were discussed in Section 5.1.1) earlier. For the long die we have assumed that the deformation history experienced by the melt in the abrupt contraction of the die is erased in the capillary section so that the extrudate swell values are not affected by the contraction flow. The assumption is based on the simplistic argument that the mean residence times in the long capillary $[t_{res} = (8/\dot{\gamma}_w)(L/D)]$ of 150 s and 75 s respectively for the lowest and the highest piston speeds of 0.004 mm/s and 0.08 mm/s, are larger than the characteristic relaxation time (0.01 s; see Table 1) of the LLDPE melt. As an independent check of this assumption we have compared, for one reasonably high value of flow rate, the predictions of extrudate swell profile from the capillary and from the capillary attached to an upstream axisymmetric contraction. The comparison is shown in Fig. 10 and it supports our assumption that it is enough to consider only the capillary part of the geometry for simulations of the long die. The obvious advan-

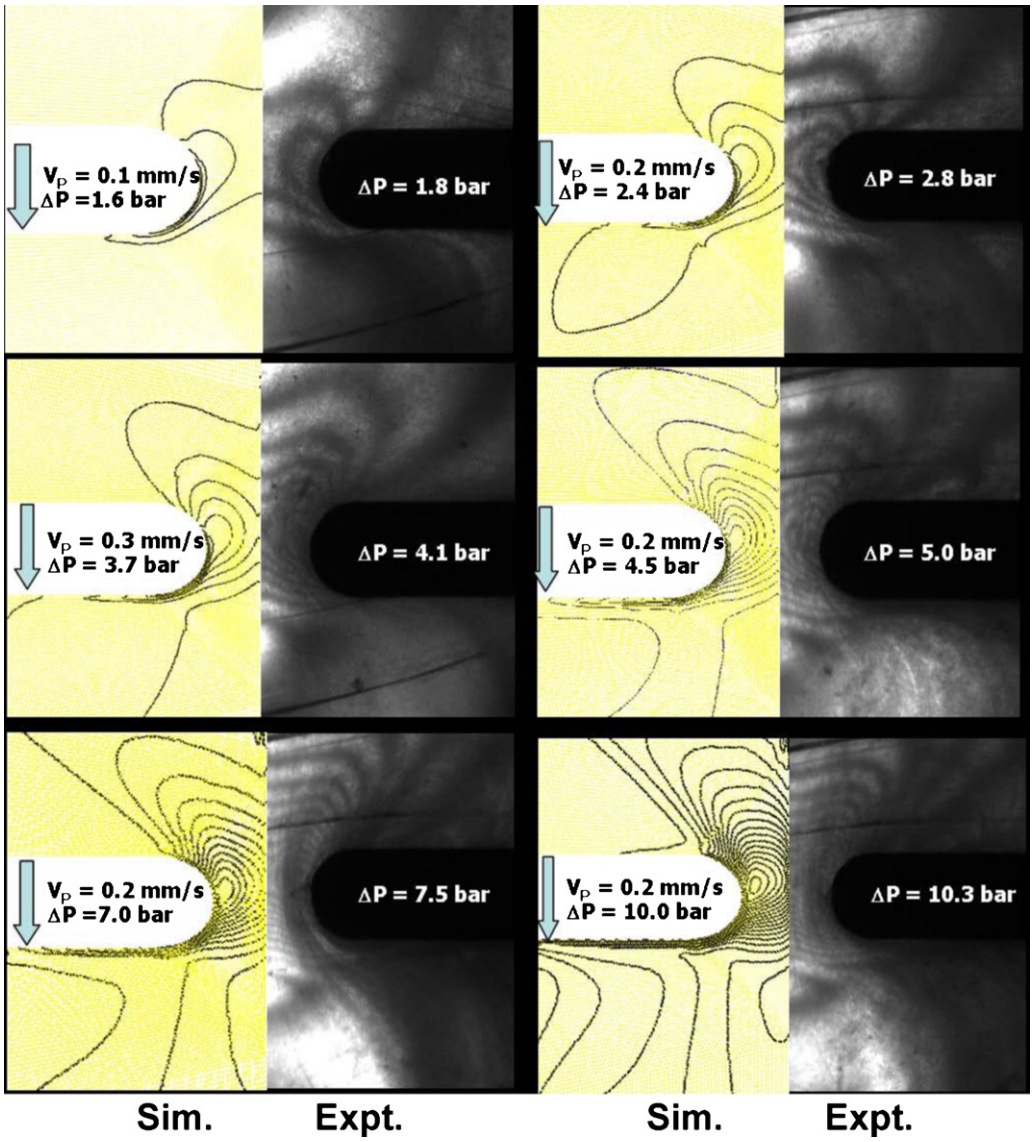

Fig. 9. Comparison between experimental birefringence patterns and those calculated from the principal stress difference contours predicted by the ALE simulations using the XPP model for LDPE 170A at 170 °C.

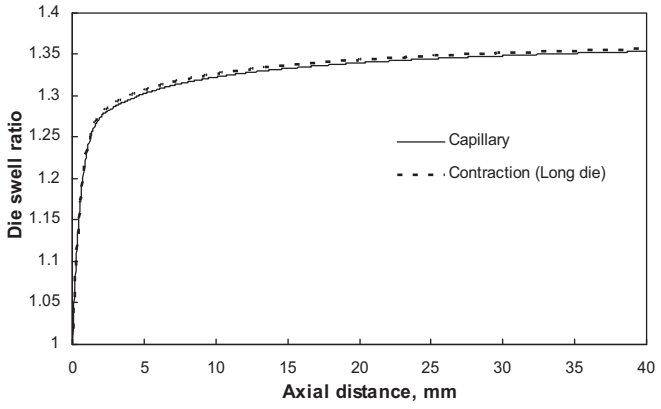

Fig. 10. Predictions of extrudate swell profile for LLDPE-2045G. The melt is extruded through the long capillary die ($L/D = 30$) and simulations are done without upstream contraction (line) and with contraction (dotted line) at an apparent shear rate of 16 s^{-1}.

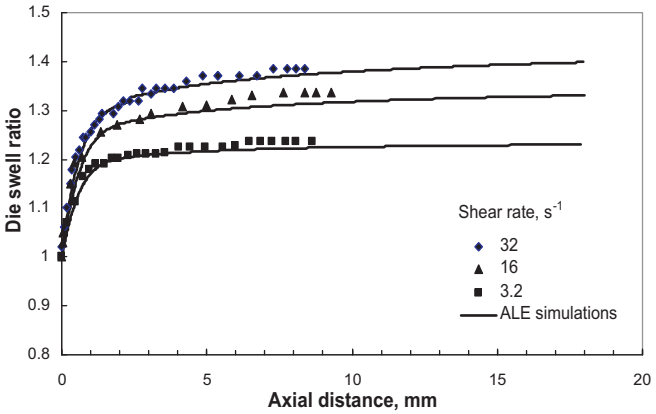

Fig. 11. Comparison between experimentally observed (symbols) and simulated (lines) extrudate swell profiles for the LLDPE-2045G melt extruding through the long die.

Table 5
Equilibrium extrudate swell comparisons for LLDPE-2045.

Shear rate (s^{-1})	Extrudate (die) swell ratio			
	Long die		Short die	
	Simulation	Experiment	Simulation	Experiment
1.6	1.23	1.24	1.26	1.30
3.2	1.24	1.31	1.29	1.35
16	1.36	1.44	1.40	1.49
32	1.40	1.51	1.46	1.56

tage of this assumption is a significant reduction in computing time. The simulation results for the capillary die are shown in Fig. 11 for three different shear rates along with the experimental data. It can be seen that our ALE based predictions of extrudate swell profile are in good agreement with the experimental measurements over the entire range of shear rates investigated here.

Note that while simulations were done assuming isothermal flow conditions, the experiments involved extrusion of melt in ambient air. A crude engineering estimate suggests that non-isothermal effects will become important when the ratio of the characteristic times for cooling by conduction in the extrudate and flow of the extrudate namely, $R^2V_e/\alpha L \approx 1$. Here, R is the radius of the extrudate, V_e is velocity of the extrudate, α is the thermal diffusivity of the melt and L is the flow length away from the die. For typical values of $R = 1$ mm, $V_e = 0.4$ mm/s and $\alpha = 10^{-3}$ cm^2/s for polyethylene melt [35] the non-isothermal effects are estimated to become significant at a distance of 4 mm away from the die exit. This estimate matches with our experimental observation of a freeze line at roughly this distance from the die exit. Therefore although the extrudate close to the die exit can be at the same temperature as the melt inside the rheometer barrel, non-isothermal effects are expected to become important further away from the exit. Hence, the predicted extrudate swell away from the die exit was also compared with experimentally determined equilibrium swell. The results are summarized in Table 5. It can be seen that for the long die the predictions match well (within 1–3%) with experiments at the lower shear rates but under-predict the equilibrium swell at higher shear rates (by 5–7%). The deviation from experimental values is most likely caused by exclusion of the upstream contraction flow from simulations. This can be seen in Fig. 10 also where inclusion of the contraction flow causes a small increase in the predicted swell. The increased swell is caused by slow relaxing modes in the melt (see relaxation spectrum in Table 3) which may not fully relax the stresses created during the upstream contraction flow especially at higher shear rates.

5.3.1.2. Extrudate swell from a short capillary die with an upstream axisymmetric contraction. We now compare the simulation results with the experimental data for the extrusion of LLDPE melt through a short capillary die having length to diameter ratio (L/D) = 10 and diameter $D = 2$ mm. Although the mean residence time of flow in this capillary is also greater than the characteristic relaxation time of LLDPE we chose to perform simulations for the entire geometry comprising the capillary and the upstream contraction. This was because the difference between the simulated extrudate swell and the experimental equilibrium swell was significant for the LDPE melt as will be discussed later. For the LLDPE melt, the difference in the swell profile between the entire geometry and only capillary is almost negligible as seen in Fig. 12. The results of simulations are shown in Fig. 13 together with the experimental swell profiles. Comparison is also made between the simulated steady state swell and the equilibrium swell (Table 5). As in the case of the long die our predictions match well with the experiments (within 3%) at lower shear rates but under-predict the equilibrium swell (by 5%) at higher shear rates with the experimental error.

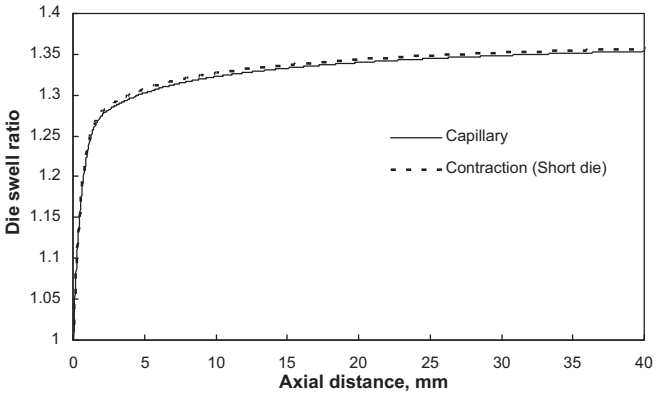

Fig. 12. Extrudate swell profile for the LLDPE-2045G melt through short capillary ($L/D = 10$) without contraction (line) and with contraction (dotted line) at 16 s^{-1}.

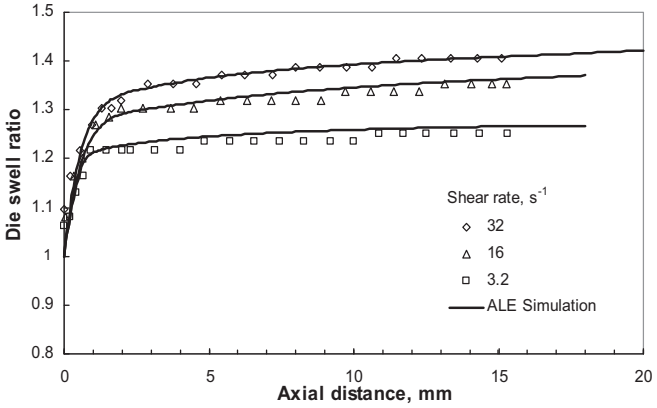

Fig. 13. Comparison between experimentally observed (symbols) and simulated (lines) extrudate swell profiles for LLDPE-2045G melt through short die.

5.3.2. Branched LDPE-170A

As noted earlier the single equation XPP model was incorporated in the ALE code to simulate the flow of LDPE-170A melt and the results of extrudate swell for long and short dies are presented below.

5.3.2.1. Extrudate swell predictions for long and short capillary dies. Simulations for the long die were once again performed without considering the upstream contraction assuming that the deformation history experienced by the melt in the abrupt contraction section upstream of the long capillary is erased in the capillary section. On the other hand the entire flow geometry was considered for simulating flow through the short die. To verify this assumption swell simulations were performed for extrusion through the long and the short capillary dies at a shear rate of 32 s^{-1} in the presence and absence of the upstream abrupt contraction. The results shown in Fig. 14 suggest that inclusion of the upstream contraction was important for the short die but not for the long die.

In general for a given die, the experimentally measured extrudate swell of LDPE-170A was higher than that of LLDPE-2045 at the same apparent wall shear rate and temperature. This may be expected because LDPE shows higher first normal stress difference than LLDPE at the same wall shear rate and temperature, and it has a broader relaxation spectrum compared to LLDPE. Additionally, LDPE melt shows strong elongation hardening character. Hence stresses built up during the contraction flow upstream of the capillary exit do not relax completely as the melt reaches the capillary exit. Subsequent relaxation of the stresses in the free surface flow causes higher swell. This is also responsible for the experimental

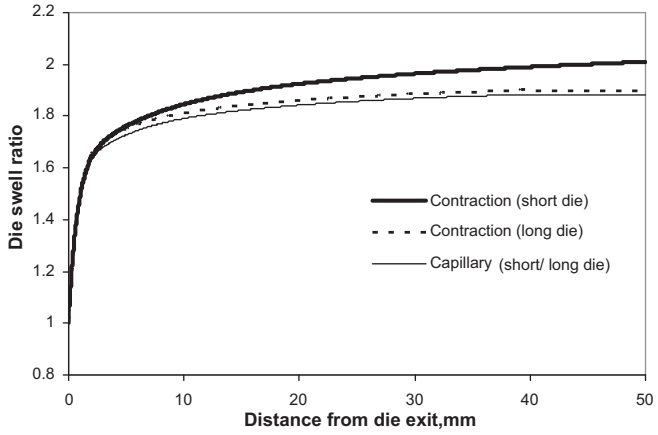

Fig. 14. Predictions of extrudate swell profiles for the LDPE-170A melt flowing at an apparent wall shear rate of 32 s^{-1} through long ($L/D = 30$) and short ($L/D = 10$) capillaries (thin line), long capillary + upstream contraction (dashed line), and short capillary + upstream contraction (thick line).

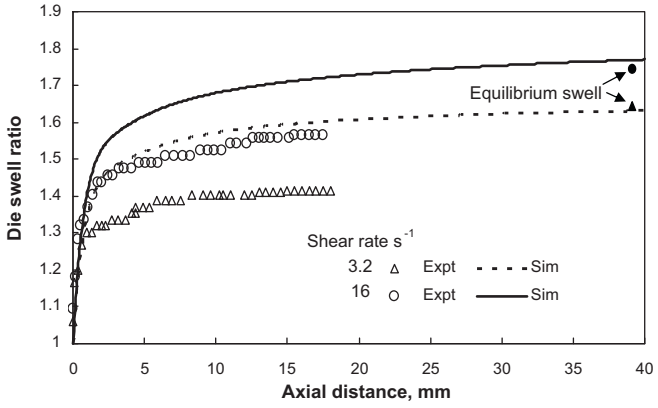

Fig. 15. Simulated transient extrudate swell profile for the LDPE-170A melt through long die; comparison with experiments.

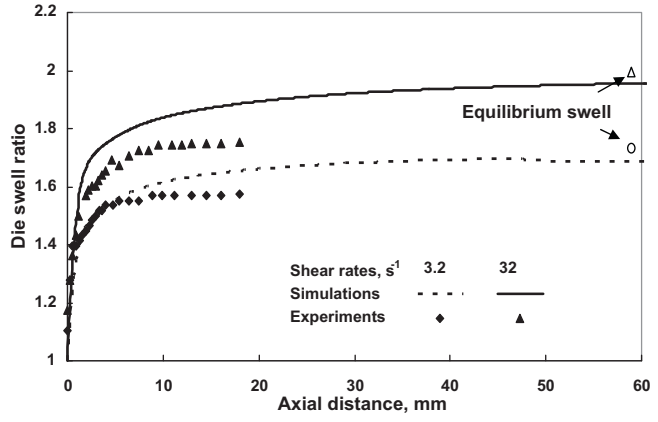

Fig. 16. Simulated transient extrudate swell profile for the LDPE-170A melt through short die; comparison with experiments.

observation of higher swell from the short die compared to the long die at the same apparent wall shear rate and temperature. Results of the ALE simulations for extrudate swell profiles are compared with experimentally obtained swell profiles for the long die and the short die in Figs. 15 and 16, respectively. While the simulations qualitatively show the same trend as observed experimentally they over-predict the swell by a substantial amount for both long and short dies. On the other hand the simulated steady state swells for

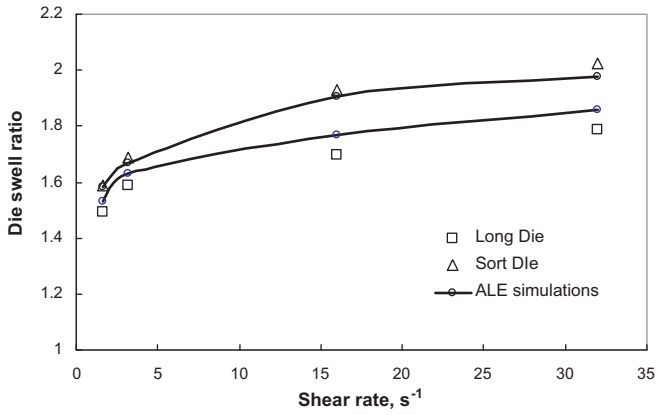

Fig. 17. Predicted equilibrium extrudate swell and comparison with experiments for the LDPE-170A melt.

both long and short dies match well with the experimentally measured equilibrium swells over the entire range of shear rates probed here (Figs. 17). These observations may be explained as follows. In the case of the experiments, which were conducted under non-isothermal conditions, the extrudate cools down in ambient air as it exits the die. Cooling increases the relaxation times and therefore traps unrelaxed stresses in the extrudate thus restricting swell. On the other hand the simulations assume isothermal flow so that at long lengths from the die exit the stresses relax completely and the swell reaches its equilibrium value. Hence while the simulations over-predict the swell profile observed under non-isothermal experimental conditions, they correctly predict the experimental equilibrium swell values.

6. Conclusions

We have successfully incorporated the single-equation multimode XPP constitutive relation in our fractional step ALE algorithm and simulated the flow of a long chain branched polyethylene (LDPE) through a two-dimensional contraction–expansion slit and the swelling of the LDPE melt upon extrusion through long and short dies. Predictions were compared with experimental flow-birefringence data in a quasi-two dimensional contraction–expansion slit die of a MultiPass Rheometer (MPR). The ALE predictions were also compared with the experimental extrudate swell profile as well as equilibrium swell measurements. Experimental data was also generated for a linear polyethylene (LLDPE) melt and simulations were performed using the PTT constitutive equation to model the rheology of this polymer. The predicted contours of birefringence, assuming the validity of the stress–optical law, were in qualitative agreement with the experimentally observed birefringence patterns for both polymers. Also, the predicted steady state pressure drop across the die was in good agreement with experimental data. The simulation results for extrudate swell profile of LLPDE melt through long and short dies were in good agreement with experimentally measured swell profile. The equilibrium swell of LLDPE was only slightly higher than the steady state swell measured during the extrusion experiments. For the LDPE melt, the simulations considerably over-predicted the experimentally observed swell profile. However, the simulated values of the final swell were in good agreement with the measured equilibrium swell. It was argued that the presence of slow relaxing modes in the LDPE and the non-isothermal experimental conditions slow down stress relaxation process considerably during extrusion. The extrudate is therefore unable to reach equilibrium swell before solidifying. However, upon heating to high temperature the trapped stresses in the extrudate relax further and

reach equilibrium swell which matches with the swell predicted from isothermal simulations.

Acknowledgments

We acknowledge Dr. Teresa Karjala's support in donating the Dow PE samples for experimental purposes and Dr. (Mrs.) Dhoble and Dr. Mohandas respectively for helping with HTGPC and NMR experiments.

References

[1] D. Rajagopalan, R.C. Armstrong, R.A. Brown, Comparison of computational efficiency of flow simulations with multimode constitutive equations: integral and differential models, J. Non-Newton. Fluid Mech. 46 (1993) 243–273.
[2] P.T. Baaijens, S.H.A. Seelen, H.P.W. Baaijens, G.W.M. Peters, H.E.H. Meijer, Viscoelastic flow past a confined cylinder of a low density polyethylene melt, J. Non-Newton. Fluid Mech. 68 (1997) 173–203.
[3] M.H. Wagner, Analysis of time-dependent non-linear stress-growth data for shear and elongational flow of a low-density branched polyethylene melt, Rheol. Acta 15 (1976) 136–142.
[4] A.C. Papanastasiou, L.E. Scriven, C.W. Macosko, An integral constitutive equation for mixed flows: viscoelastic characterization, J. Rheol. 27 (1983) 387–410.
[5] T.C.B. McLeish, R.G. Larson, Molecular constitutive equations for a class of branched polymers: the Pom–Pom polymer, J. Rheol. 42 (1998) 81–110.
[6] A.E. Likhtman, R.S. Graham, Simple constitutive equation for linear polymer melts derived from molecular theory: Rolie-Poly equation, J. Non-Newton. Fluid Mech. 114 (2003) 1–12.
[7] R.I. Tanner, A theory of die-swell revisited, J. Non-Newton. Fluid Mech. 129 (2005) 85–87.
[8] X.-L. Luo, R.I. Tanner, A streamline finite element scheme for solving viscoelastic flow problems. Part II. Integral constitutive models, J. Non-Newton. Fluid Mech. 22 (1986) 61–89.
[9] X.-L. Luo, R.I. Tanner, Finite element simulation of long and short circular die extrusion experiments using integral models, Int. J. Numer. Methods Eng. 25 (1988) 9–22.
[10] X.-L. Luo, E. Mitsoulis, Memory phenomena in extrudate swell simulations from annular dies, J. Rheol. 33 (1989) 1307–1327.
[11] X.-L. Luo, E. Mitsoulis, An efficient algorithm for strain history tracking in finite element computations of non-newtonian fluids with integral constitutive equations, Int. J. Numer. Methods Fluids 11 (1990) 1015–1031.
[12] X.-L. Luo, E. Mitsoulis, A numerical study of the effect of elongational viscosity on vortex growth in contraction flows of polyethylene melts, J. Rheol. 34 (1990) 309–342.
[13] A. Goublomme, B. Draily, M.J. Crochet, Numerical prediction of extrudate swell of a high-density polyethylene, J. Non-Newton. Fluid Mech. 44 (1992) 171–195.
[14] A. Goublomme, M.J. Crochet, Numerical prediction of extrudate swell of a high-density polyethylene: further results, J. Non-Newton. Fluid Mech. 47 (1993) 281–287.
[15] D.G. Kiriakidis, E. Mitsoulis, Viscoelastic simulations of extrudate swell for an HDPE melt through slit and capillary dies, Adv. Polym. Technol. 12 (1993) 107–117.
[16] R. Ahmed, R. Liang, M.R. Mackley, The experimental observation and numerical prediction of planar entry flow and die swell for molten polyethylene, J. Non-Newton. Fluid Mech. 59 (1995) 129–153.
[17] C. Béraudo, A. Fortin, T. Coupez, Y. Demay, B. Vergnes, J.-F. Agassant, A finite element method for computing the flow of multi-mode viscoelastic fluids: comparison with experiments, J. Non-Newton. Fluid Mech. 75 (1998) 1–23.
[18] G.B. Bishko, O.G. Harlen, T.C.B. McLeish, T.M. Nicholson, Numerical simulation of the transient flow of branched polymer melts through a planar contraction using the 'Pom–Pom' model, J. Non-Newton. Fluid Mech. 82 (1999) 255–273.
[19] K. Lee, M.R. Mackley, T.C.B. McLeish, T.M. Nicholson, O.G. Harlen, Experimental observation and numerical simulation of transient stress fangs within flow in molten polyethylene, J. Rheol. 45 (2001) 1261–1277.
[20] W.M.H. Verbeeten, G.W.M. Peters, F.P.T. Baaijens, Differential constitutive equations for polymer melts: the eXtended Pom–Pom model, J. Rheol. 45 (2001) 823–843.
[21] N. Clemeur, R.P.G. Rutgers, B. Debbaut, Numerical simulation of abrupt contraction flows using the Double Convected Pom–Pom model, J. Non-Newton. Fluid Mech. 117 (2004) 193–209.
[22] POLYFLOW User's Manual, Ver. 3.10.0, Fluent Inc., Lebanon New Hampshire, 2003.
[23] M.J. Crochet, B. Debbaut, R. Keunings, J.M. Marchal, Polyflow: a multi-purpose finite element program for continuous polymer flows, in: K.T. O'Brien (Ed.), Applications of CAE in Extrusion and Other Continuous Processes, Carl Hanser Verlag, München, 1992.
[24] G. Russo, T.N. Phillips, Numerical prediction of extrudate swell of branched polymer melt, Rheol. Acta 49 (2010) 657–676.
[25] J. Meissner, Basic parameters, melt rheology, processing and end-use properties of three similar low density polyethylene samples, Pure Appl. Chem. 42 (1975) 552–612.
[26] X. Yang, S. Wang, C. Chai, Extrudate swell behaviour of polyethylenes: capillary flow, wall slip, entry/exit effects and low temperature anomalies, J. Rheol. 42 (1998) 1075–1094.
[27] V. Ganvir, A. Lele, R. Thaokar, B.P. Gautham, Simulation of viscoelastic flows of polymer solutions in abrupt contractions using an arbitrary Lagrangian Eulerian (ALE) based finite element method, J. Non-Newton. Fluid Mech. 143 (2007) 157–169.
[28] V. Ganvir, A. Lele, R. Thaokar, B.P. Gautham, Predictions of extrudate swell in polymer extrusion using an arbitrary Lagrangian Eulerian (ALE) based finite element method, J. Non-Newton. Fluid Mech. 156 (2009) 21–28.
[29] R.C. Randall, E.T. Hsieh, 13C NMR in Polymer Quantitative Analyses, NMR and Macromolecules ACS Symposium Series, vol. 247, 1984, pp. 131–151 (Chapter 9).
[30] M.R. Mackley, R.T.J. Marshall, J.B.A.F. Smeulders, The multipass rheometer, J. Rheol. 39 (1995) 1293–1309.
[31] M.W. Collis, A.K. Lele, M.R. Mackley, R.S. Graham, D.J. Groves, A.E. Likhtman, T.M. Nicholson, O.G. Harlen, T.C.B. McLeish, L. Hutchings, C.M. Fernyhough, R.N. Young, Constriction flows of monodisperse linear entangled polymers: multiscale modelling and flow visualization, J. Rheol. 49 (2005) 501–522.
[32] C.W. Macosko, Rheology Principles, Measurements, and Applications, Wiley-VCH, Inc., 1994.
[33] W.M.H. Verbeeten, G.W.M. Peters, F.P.T. Baaijens, Numerical simulations of the planar contraction flow for a polyethylene melt using the XPP model, J. Non-Newton. Fluid Mech. 117 (2004) 73–84.
[34] D.C. Huang, J.L. White, Extrudate swell from slit and capillary dies: an experimental and theoretical study, Polym. Eng. Sci. 19 (1979) 609–616.
[35] T. Hashimoto, T. Tsuji, Thermal diffusivity measurements of polyethylene melt by a new temperature wave method, J. Therm. Anal. Calorim. 40 (1993) 721–726.